Resolving the spin polarization and magnetic domain wall width of $(Nd,Dy)_2Fe_{14}B$ with spin-polarized scanning tunneling microscopy

Toshio Miyamachi[1,2*], Christoph Sürgers[3], and Wulf Wulfhekel[3,4]

[1]*Institute of Materials and Systems for Sustainability (IMaSS), Nagoya University, Furo cho, Chikusa ku, Nagoya, Aichi 464 8601, Japan*
[2]*Graduate School of Engineering and School of Engineering, Nagoya University, Furo cho, Chikusa ku, Nagoya, Aichi 464 8603, Japan*
[3]*Physikalisches Institut, Karlsruhe Institute of Technology (KIT), Wolfgang Gaede Strasse 1, 76131 Karlsruhe, Germany*
[4]*Institute for Quantum Materials and Technologies, Karlsruhe Institute of Technology (KIT), 76021 Karlsruhe, Germany*

[*]E mail: toshio.miyamachi@imass.nagoya u.ac.jp

The electronic structure and the domain wall width of industrial $(Nd,Dy)_2Fe_{14}B$ hard magnets were investigated using low temperature, spin polarized scanning tunneling microscopy (STM) in ultra high vacuum. In a first step, atomically clean and flat surfaces were prepared. The flat terraces were separated by monatomic steps. Surface termination was identified as the Fe c layer from atomically resolved STM imaging. The electronic density of states and its spin polarization agree well with ab initio predictions of the Fe c layer. High resolution spin polarized STM images allowed to finally resolve the domain wall width w of only 3.2 ± 0.4 nm.

The ternary alloys of Nd Fe B with their stable phase $Re_2Fe_{14}B$ (Re, rare earth) stand out among the hard permanent magnets.[1] They combine the high magnetocrystalline anisotropy of the heavy Re elements with the large magnetization density of the 3d transition metal Fe, reaching record values of the energy product at ambient temperatures. They also combine the most abundant magnetic 4f and 3d elements leading to competitive costs of production. In many applications they have replaced other materials, reducing the size and weight but boosting the efficiency of motors, actuators and generators. Dy doping of $Nd_2Fe_{14}B$ increases the coercivity, improving stability for electromotor applications, for example. Two ways to produce $Nd_2Fe_{14}B$ and doped variants at competitive costs have been developed: (a) rapid solidification, i.e. melt-spinning, followed by hot pressing and deformation and (b) powder metallurgy combined with thermal treatment. While the former is more expensive, it can result in superior material properties.

The relation between the microscopic grain structure and the magnetic properties has been studied in detail to optimize the material for different applications. Here, the key property is that demagnetization by nucleation of magnetic domains and domain wall propagation is suppressed.[1,2] Important ingredients for these mechanisms are the energy and width of 180° domain walls. Unsurprisingly, this has motivated high-resolution magnetic imaging of the domain walls by different techniques. The technique that so far has given the most precise domain wall width is transmission electron microscopy, which can reach a lateral resolution in the range of few nanometers.[3] The extremely high magnetic anisotropy K of the material in combination with a moderate magnetic exchange A, however, results in an expected domain wall width $w \approx 2\sqrt{A/K}$ in the nanometer range,[4] rendering a precise determination of the wall width difficult. Spin-polarized scanning tunneling microscopy (Sp-STM) has been used to measure extremely narrow domain walls in atomically thin films on surfaces,[5–7] where magnetic anisotropies can be orders of magnitude larger than in bulk samples and exchange constants may be reduced. In this letter we resolved the domain wall in commercial Dy-doped $Nd_2Fe_{14}B$ samples using the high lateral resolution of Sp-STM. The results represent the first precise real-space

determination of the wall width in this material and also the first Sp-STM experiment carried out on commercial hard magnet products. Additionally, we determined the electronic density of states and its spin polarization of the material as a function of electron energy.

The $(Nd, Dy)_2Fe_{14}B$ sample in this study is a nanocrystalline bulk magnet made from rapidly quenched melt-spun ribbons. The nanocrystalline ribbons were crushed into powders and sintered at around 600 °C under pressure. The hot-pressed $(Nd, Dy)_2Fe_{14}B$ magnet was subsequently hot-deformed at 650 700 °C to develop the strong (001) texture. The atomic composition ratio of Nd and Dy was evaluated by scanning electron microscopy with energy dispersive X-ray spectroscopy (SEM-EDX) to be $(Nd_{1 x},Dy_x)_2Fe_{14}B$ with $x = 0.07 \pm 0.03$. The sample was cut, polished and finally fixed on the STM sample holder followed by introduction into the ultra-high vacuum (UHV). While STM and its spin-polarized variant are very powerful techniques with high lateral and energy resolution[8–11] they are extremely surface sensitive and only probe the evanescent electronic states of the sample that leak into the vacuum.[12] As the samples were exposed to the ambient air, in a first step the oxidized surface layer has to be removed and atomically clean and flat surfaces need to be prepared. This was done by cycles of Ar^+ sputtering followed by annealing. The samples were then transferred in situ to a low-temperature STM[13] operating in these experiments at ≈4.2 K. The STM tips were etched from a W wire followed by flashing in UHV to remove the natural oxide. Topographic STM images were taken in the constant-current mode. Differential conductance spectra were recorded using a lock-in technique with modulation of 20 mV at a frequency of 751 Hz. For this, a feedback loop was opened keeping the tip sample distance constant while ramping the voltage. Maps of the differential conductance were obtained by recording the dI/dV signal while scanning the surfaces in constant-current mode. Spin-polarized tips were produced by dipping the W tip into the $(Nd,Dy)_2Fe_{14}B$ sample and giving voltage pulses to transfer some material from the sample to the tip. This was repeated until a sharp tip was obtained that displayed a spin contrast.[14]

Figure 1 summarizes the sample preparations results. At annealing temperatures of 400 °C, the surface is conductive
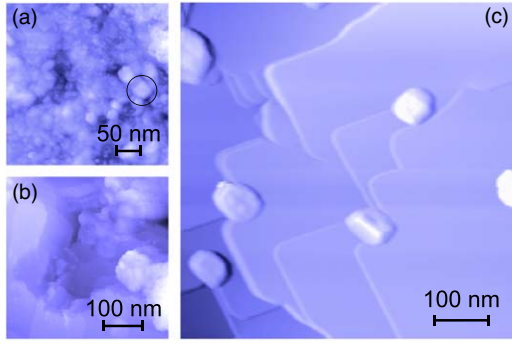
Fig. 1. (Color online) STM topography of the sample surface after Ar^+ sputtering and post annealing to 400 °C (a), 500 °C (b) and 600 °C (c), illustrating grain coarsening and flattening of the surface with rising annealing temperature. The circle in (a) indicates an atomically flat region or grain of fourfold symmetry. STM images are recorded at I 100 pA, V 1 V.

and STM images could be taken revealing a high degree of disorder and roughness. However, atomically flat areas first developed as indicated by the circle in Fig. 1(a). These are probably individual crystalline grains with diameters of around 50 nm. The square shape already indicates the development of a crystal texture at the surface. Increasing the annealing temperature to 500 °C leads to a coarsening of the crystalline grains [see Fig. 1(b)], until at 600 °C large and atomically flat terraces finally dominate the surface [see Fig. 1(c)]. Furthermore, this coarsening agrees qualitatively with prior results.[15] The steps separating the terraces show angles of 90°, again indicating texturing with two unit vectors of the tetragonal unit cell of $(Nd,Dy)_2Fe_{14}B$ being in the plane of the surface. Note from the X-ray diffraction (XRD) pattern after annealing that the bulk crystal structure of $(Nd,Dy)_2Fe_{14}B$ remains unchanged in a series of surface preparation procedures (see supplementary data Fig. S1 available online at stacks.iop.org/APEX/14/115504/mmedia).

Figure 2(a) shows the bulk unit cell of $Nd_2Fe_{14}B$ with its inequivalent Fe and Nd sites as well as the B site.[16,17] The lattice parameters are $a = 0.880$ nm and $c = 1.219$ nm. In order to determine the orientation of the crystalline grains, we analyze the step heights between neighboring atomically flat terraces [see Fig. 2(b)]. Taking line sections, a step height of ≈ 1.25 nm can be deduced from the images [see Fig. 2(c)]. This suggests that the c-axis is normal to the surface plane and the square plane with lattice constant a is in the plane, which also explains the observed angles between the steps. Moreover, the line scans indicate that the steps are of a full unit cell height, i.e. the same part of the bulk unit cell always resides at the surface. In order to get information on the top atoms at the surface, STM images with atomic resolution were taken as depicted in Fig. 2(d). A square lattice with a lattice constant of ≈ 0.6 nm is resolved [see also line scan of Fig. 2(e)]. This is near $1/\sqrt{2}$ the size of the in-plane lattice constant a, i.e. the observed atoms sit in square symmetric positions and contain two atoms per in-plane unit cell. Compared with the bulk crystal structure, this surface unit cell agrees with the Fe c atomic positions [pink balls in Fig. 2(a)], suggesting a surface termination by this layer. With identification of the grain orientation, we can conclude that the observed straight step edges run along $\langle 110 \rangle$ directions.

To further investigate the termination and learn about the electronic densities as well as their spin polarization, we performed spin-polarized scanning tunneling spectroscopy on large, atomically flat terraces. The dI/dV curves are recorded between -2.6 and 1.6 V, spanning a large energy range around the Fermi energy E_F of both occupied and unoccupied states. Due to the tunneling magnetoresistance (TMR) effect, the spectra depend on the relative orientation of the sample and tip magnetization.[18] Figure 3 summarizes the results showing tunneling spectra, topography and spin-polarized STM images. In Fig. 3(a) we show the obtained spin-polarized dI/dV curves using tips dipped into the $(Nd,Dy)_2Fe_{14}B$ substrate. Red and blue curves indicate spectra recorded on two oppositely magnetized magnetic domains of $(Nd,Dy)_2Fe_{14}B$ on the left and right side, respectively, as shown in Fig. 3(d). Due to the large magnetocrystalline anisotropy of the material, domains are magnetized either parallel to the c-axis of the crystal structure (for $Dy_2Fe_{14}B$ and for $Nd_2Fe_{14}B$ above ≈ 130 K), i.e. the magnetization points into or out of the surface plane, or somewhat canted from this direction (for $Nd_2Fe_{14}B$ below ≈ 130 K) as discussed in all detail in the literature.[19–21] Figure 3(d) shows the topography of the atomically flat grain together with the corresponding maps of the spin-polarized dI/dV signal at indicated sample bias voltages. Clearly, two oppositely magnetized domains separated by a domain wall can be seen. The domain wall runs through the grain, i.e. the grain is larger than the single domain limit[22–24] as a consequence of the annealing and coarsening. Before analyzing the domain wall, we return to discuss the details of the voltage dependence of the spin polarization.

As seen in Fig. 3(a), the dI/dV spectra on the two domains show an overall similar behavior, with two peaks at negative sample bias (at -1.8 and -1.1 V) and one for positive at $+0.6$ V, but differ slightly indicating a spin polarization. Moreover, while at negative bias voltages, the red curve recorded on the left domain shows higher conductivities than that for the right, the contrast reverses for positive bias. Tunneling spectra contain information on the density of states of the sample as described by Tersoff and Hamann.[12,25] To first order, the dI/dV signal is proportional to the local density of states (LDOS). At higher orders, and especially outside the low-bias approximation, the voltage-dependent transmission probability for the electrons also enters dI/dV. In order to correct for this, we fitted the typical transmission function[26] to the high-voltage parts of the dI/dV curves [dotted black lines in Fig. 3(a)] and normalized dI/dV by this transmission, resulting in the spectra displayed in Fig. 3(b). This signal better represents the LDOS and all the features observed in the raw data are retrieved, i.e. two peaks below and one peak above E_F. When we compare the measured behavior of the differential conductance peaks at about $+0.6$, -1.1 and -1.8 V with first-principles calculations[27] of the LDOS and for the different Fe sites in pure $Nd_2Fe_{14}B$, we find best agreement for a surface termination of the substrate with Fe c sites, in accord with the observation of the topography. Moreover, the calculations indicated that the individual peaks (and their spin polarization) are caused by the different Fe d-states, which are also responsible for the magnetic moment of Fe in the different sites. As depicted in Fig. 3(c), we computed the asymmetry from the normalized spectra, i.e.
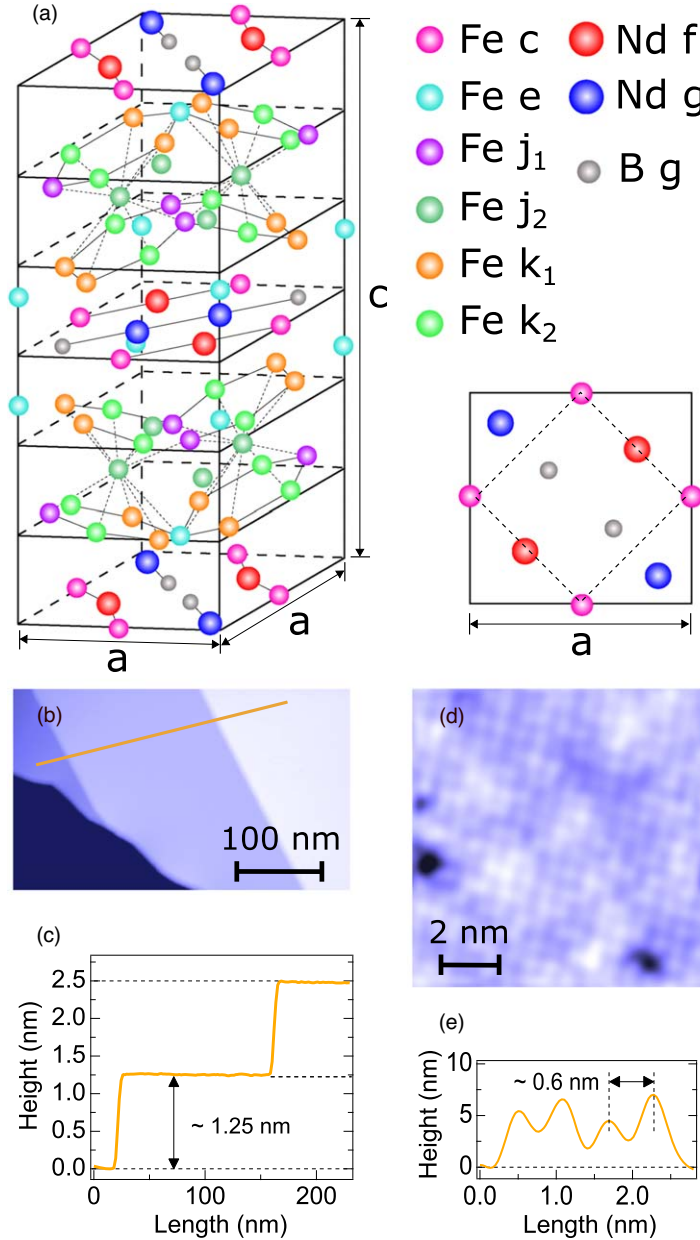
Fig. 2. (Color online) (a) Schematics of the bulk crystal structure and *ab* plane structure of the Fe c layer of $Nd_2Fe_{14}B$. Dashed lines in the right figure indicate a Fe Fe distance of 0.62 nm. (b) STM image of an atomically clean region of the surface with step edges recorded at I 100 pA, V 1 V. (c) Line scan along the orange line in (b) revealing a step height of ≈1.25 nm corresponding to the *c* axis unit cell height. (d) Atomically resolved STM image of the surface showing a square symmetry recorded at I 100 nA, V 10 mV. The distance between the observed atoms is ≈0.6 nm [see line scan in (e)] corresponding to the distance and square symmetry of the Fe atoms in the c layer.

the difference over the sum of the normalized spectra, which is proportional to the spin polarization of the LDOS. The values vary with voltage in the range of ±5% and change sign near E_F. Note that the measured spin polarization is that of the tunneling current and not directly of the sample. It is a product of the spin polarizations of the tip and the sample.[10,11,18] If we assume the spin polarization of the tip to be identical to that of the sample, the LDOS of the sample has a spin polarization varying in the ±25% range. The ab initio calculations predicted a sign reversal of the spin polarization near E_F, in agreement with our experimental observations.

After focusing on the LDOS and its spin polarization, we finally use the high lateral resolution of Sp-STM to determine the width of the magnetic domain walls inside the grain.

Figure 4 shows the line profile of the spin-polarized *dI/dV* signal at −1.1 V across the domain wall shown by the green line in Fig. 3(d). The best signal-to-noise ratio was achieved at this voltage. Clearly, the signal shows a sharp transition between the two domains. Fitting the data with the usual $\tanh(2x/w)$ wall profile of Bloch walls[4,28] results in a wall width w of 3.2 ± 0.4 nm. The voltage-dependent domain wall profiles at 0.6 and −1.8 V shown in the supplementary data (Fig. S2) give comparable w values of 3.6 ± 0.6 and 3.4 ± 0.4 nm, respectively. This ensures high reliability of domain wall widths evaluated in this work. Note that w corresponds to the full width of the wall (see Ref. 4). The measured widths agree well with transmission electron microscopy estimates of the full wall width between 2 and 10 nm (see Ref. 3) but the superior lateral resolution of
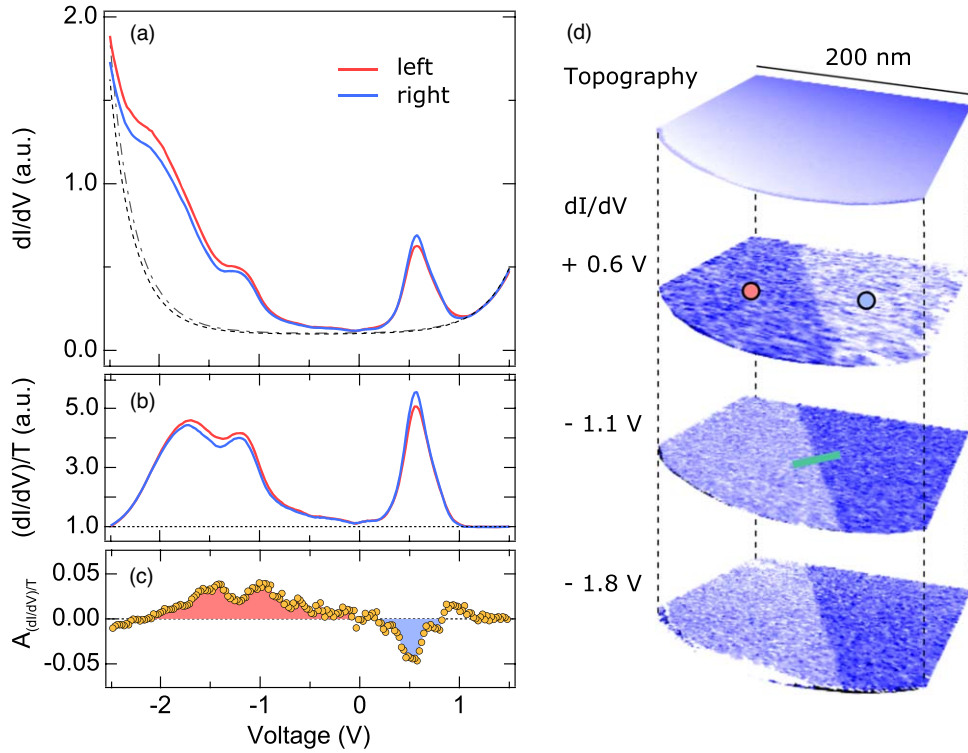
Fig. 3. (Color online) (a) Differential conductance dI/dV measured with a spin polarized tip on two magnetic domains (blue and red curves) together with the fitted tunneling transmission functions (dashed gray curves). The STM tip is stabilized at I 500 pA, V 1.5 V. (b) Spin polarized dI/dV spectra normalized for the tunneling transmission. (c) Asymmetry of the normalized differential conduction, which is proportional to the spin polarization. (d) STM topography of an atomically flat grain together with maps of the local dI/dV signal at indicated bias voltages showing two magnetic domains. The contrast reverses as function of bias voltage, illustrating the reversal of spin polarization. The STM image is recorded at I 500 pA, V 0.6 V.
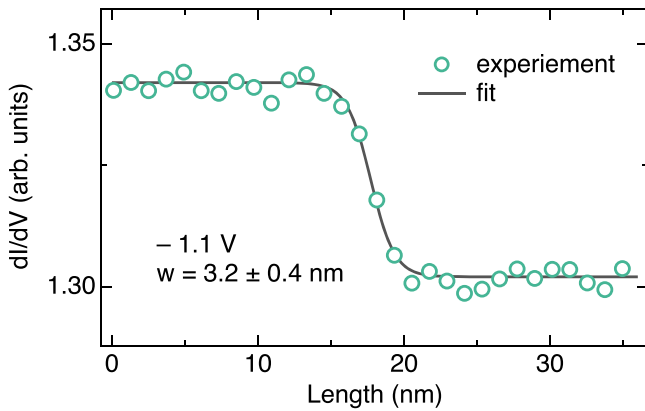
Fig. 4. (Color online) Differential conductance dI/dV signal measured with a spin polarized tip at 1.1 V perpendicularly across the domain wall indicated by the green line in Fig. 3(d) together with a fit to the $\tanh(2x/w)$ wall profile (black line). The fitted wall width w is 3.2 ± 0.4 nm.

Sp-STM allows for a much more precise determination. The magnetic anisotropy K can be estimated from the wall width using the relation $w = 2\sqrt{A/K}$. With $A = 6.4$ pJ m^{-1} (see Ref. 29), we obtain a magnetic anisotropy K of ≈ 2.5 MJ m^{-2}, in excellent agreement with the literature.[29] Finally, the wall profile agrees well with that of Bloch walls and does not show the asymmetric shape of a Néel cap. In fact, micromagnetic calculations suggest that the bulk Bloch domain walls keep their Bloch character up to the surface.[30]

In conclusion, we have demonstrated that, with careful surface preparation, commercial hard magnets can also be investigated with the highly surface sensitive technique of Sp-STM. The high lateral resolution of this technique allowed us to dramatically reduce the uncertainty of the domain wall width in $(Nd,Dy)_2Fe_{14}B$.

1) O. Gutfleisch, M. A. Willard, E. Brück, C. H. Chen, S. G. Sankar, and J. P. Liu, Adv. Mater. **23**, 821 (2011).
2) M. K. Griffiths, J. E. L. Bishop, J. W. Tucker, and H. A. Davies, J. Magn. Magn. Mater. **183**, 49 (1997).
3) S. J. Lloyd, J. C. Loudon, and P. A. Midgley, J. Microscopy **207**, 118 (2002).
4) A. Hubert and R. Schäfer, *Magnetic Domains: the Analysis of Magnetic Microstructures* (Springer, Berlin, 1998).
5) O. Pietzsch, A. Kubetzka, M. Bode, and R. Wiesendanger, Phys. Rev. Lett. **84**, 5212 (2000).
6) M. Pratzer, H. J. Elmers, M. Bode, O. Pietzsch, A. Kubetzka, and R. Wiesendanger, Phys. Rev. Lett. **87**, 127201 (2001).
7) S. Bodea, W. Wulfhekel, and J. Kirschner, Phys. Rev. B **72**, 100403 (2005).
8) G. Binnig, H. Rohrer, Ch. Gerber, and E. Weibel, Phys. Rev. Lett. **49**, 57 (1982).
9) G. Binnig, H. Rohrer, Ch. Gerber, and E. Weibel, Phys. Rev. Lett. **50**, 120 (1983).
10) R. Wiesendanger, Rev. Mod. Phys. **81**, 1495 (2009).
11) W. Wulfhekel and J. Kirschner, Annu. Rev. Mater. Res. **37**, 69 (2007).
12) J. Tersoff and D. R. Hamann, Phys. Rev. B **31**, 805 (1985).
13) L. Zhang, T. Miyamachi, T. Tomanic, R. Dehm, and W. Wulfhekel, Rev. Sci. Instrum **82**, 103702 (2011).
14) T. K. Yamada, M. M. J. Bischoff, T. Mizoguchi, and H. van Kempen, Appl. Phys. Lett. **82**, 1437 (2003).
15) V. Neu, S. Melcher, U. Hannemann, S. Fähler, and L. Schultz, Phys. Rev. B **70**, 144418 (2004).

16) J. F. Herbst, J. J. Croat, F. E. Pinkerton, and W. B. Yelon, Phys. Rev. B **29**, 4176 (1984).

17) D. Givord, H. S. Li, and J. M. Moreuau, Sol. Stat. Commun. **50**, 497 (1984).

18) M. Julliere, Phys. Lett. A **54**, 225 (1975).

19) D. Givord, H. S. Li, and R. Pierre de la Bathie, Sol. Stat. Commun. **51**, 857 (1984).

20) J. M. Cadogan, J. P. Gavigan, D. Givord, and H. S. Li, J. Phys. F: Met. Phys. **18**, 779 (1988).

21) J. F. Herbst, Rev. Mod. Phys. **63**, 819 (1991).

22) A. Aharoni, IEEE Trans. Mag. **27**, 4775 (1991).

23) A. Yamasaki, W. Wulfhekel, R. Hertel, S. Suga, and J. Kirschner, Phys. Rev. Lett. **91**, 127201 (2003).

24) A. Yamasaki, W. Wulfhekel, R. Hertel, S. Suga, and J. Kirschner, J. Appl. Phys. **95**, 7025 (2003).

25) J. Tersoff and D. R. Hamann, Phys. Rev. Lett. **50**, 1998 (1983).

26) V. A. Ukraintsev, Phys. Rev. B **53**, 11176 (1996).

27) Z. Q. Gu and W. Y. Ching, Phys. Rev. B **36**, 8530 (1987).

28) L. D. Landau and E. Lifshitz, Phys. Z. Sowjet. **8**, 153 (1935).

29) J. Fischbacher, A. Kovacs, M. Gusenbauer, H. Oezelt, L. Exl, S. Bance, and T. Schrefl, J. Phys. D: Appl. Phys. **51**, 193002 (2018).

30) H. Sepehri-Amin, T. Ohkubo, and K. Hono, Mater. Trans. **57**, 1221 (2016).